JOURNAL OF GEOPHYSICAL RESEARCH, VOL. 91, NO. C2, PAGES 2289-2307, FEBRUARY 15, 1986

NEW ALGORITHMS FOR MICROWAVE MEASUREMENTS OF OCEAN WINDS: APPLICATIONS TO SEASAT AND THE SPECIAL SENSOR MICROWAVE IMAGER

Frank J. Wentz and L. A. Mattox

Remote Sensing Systems, Sausalito, California

Steve Peteherych

Atmospheric Environment Service, Downsview, Ontario, Canada

Abstract. Improved second generation normalized radar cross section (NRCS) and brightness temperature (T_B) models and associated wind retrieval algorithms are derived for the Seasat microwave radiometer SMMR and scatterometer SASS. The derivation of the NRCS model is based on the assumption of a Rayleigh distribution of wind speeds, and no in situ anemometer measurements are used. Furthermore, the NRCS model derivation is designed to preclude, as much as possible, systematic errors in the polarization and incidence angle relationships. A constant power law NRCS model is used, except for nadir observations. The nadir NRCS for winds above 15 m/s falls off faster with increasing wind speed than is predicted by a constant power law relationship. The T_B model derivation consists of finding the wind-induced emissivity coefficients, modifying the 37-GHz atmospheric absorption coefficients and removing biases in the T_B observations. The T_B biases are found to be stable except for the 18-GHz channels, which experience large, time-dependent biases. The NRCS and T_B models are incorporated into new wind retrieval algorithms, which are used to process the SASS and SMMR 3-month data sets. Small residual systematic errors in the SASS winds (±0.5 m/s or less) are found. A histogram of the SASS winds closely resembles a Rayleigh distribution. The SASS winds are compared with 1623 National Data Buoy Office (NDBO) buoy observations, and a 1.6-m/s rms discrepancy, with a -0.1-m/s bias, is found. The SASS and SMMR winds are compared on a 150-km cell-by-cell basis, giving 123,000 wind comparisons for the 3-month period. The comparisons are done using eight different combinations of three SMMR channels. Good agreement is found between the SASS and SMMR winds, except for two of the channel combinations that show little, if any, skill in retrieving wind. Over the SASS primary off-nadir swath, the SMMR and SASS wind agreement ranges from 1.3 to 2.2 m/s, depending on the channel combination. For the SMMR versus SASS nadir wind comparisons, the agreement slightly degrades. The SMMR winds appear to be more noisy than the SASS winds for winds below 3 m/s. These results indicate that the Special Sensor Microwave Imager (SSM/I), to be launched in 1986, will have the capability to measure the near-surface wind speed to an accuracy of about 2 m/s.

Paper number 5C0679.
0148-0227/86/005C-0679$05.00

Introduction

Aircraft and satellite experiments have clearly demonstrated that the wind speed near the sea surface can be remotely sensed by microwave radiometers and scatterometers [Swift, 1977; Munn, 1978; Bernstein, 1982]. The passive radiometer collects the radiation that is naturally emitted by the sea surface and intervening atmosphere, whereas the active scatterometer measures the component of transmitted power that is backscattered from the sea surface. Both the emitted and backscattered radiation are directly affected by surface roughness, which is correlated with the near-surface wind speed. The correlation between roughness and wind speed is a complex, coupled phenomenon [Kinsman, 1965] that is not currently well understood.

In this paper we focus on the wind-sensing performance of the oceanographic satellite Seasat, which observed the world's oceans from July to October 1978. The Seasat results are then used as an indicator of the wind-sensing capabilities of a new generation satellite microwave radiometer, the special sensor microwave imager (SSM/I), which will be launched in 1986. Seasat carried three wind sensors: a 14.6-GHz scatterometer SASS, a multifrequency microwave radiometer SMMR, and a 13.5-GHz altimeter. The Seasat instrumentation is thoroughly described by Weissman [1980]. The altimeter winds have been analyzed by Chelton and McCabe [1985], and we do not consider them in this paper. Also, we only consider wind speed retrievals, and the SASS wind directions are not analyzed.

The original analysis of the SASS winds consisted of comparisons with wind fields generated from in situ anemometer measurements obtained from the Joint Air Sea Interaction Experiment (JASIN) and the Gulf of Alaska Experiment (GOASEX), as is described by Jones et al. [1982], Schroeder et al. [1982], and Brown et al. [1982]. After careful tuning of the algorithm to the in situ winds, a 1.3-m/s rms difference, with no bias, was obtained for the SASS versus JASIN wind comparisons. This JASIN-derived algorithm was called SASS-I. Since the algorithm tuning involved modifying a model function with many degrees of freedom, the significance of the 1.3-m/s statistic was unclear. Furthermore, when the winds from the SASS-I algorithm were compared with the GOASEX in situ fields, the agreement was considerably poorer, being 2.7 m/s, and there was an overall 1-m/s bias, with the SASS winds being high relative to the fields. Subsequently, Weller et al. [1983] discovered problems with the JASIN buoy anemometers. The JASIN reference

anemometer W2/VAWR seemed to be biased high by about 10%. This bias in the W2/VAWR anemometer was absorbed in the SASS algorithm tuning and may partly explain why the SASS-I winds were biased high relative to the GOASEX winds.

The SASS-I algorithm was used for the original processing of the 3-month SASS data set. A statistical analysis of these original winds revealed a number of systematic errors [Wentz et al., 1984]. The winds calculated from horizontal polarization normalized radar cross-section measurements (denoted by NRCS or σ^0) were biased high relative to those coming from the vertical polarization σ^0's. Similarly, there was an artificial cross-swath wind speed gradient due to an incorrect specification of the σ^0 versus incidence angle relationship. Furthermore, the σ^0's having a low signal-to-noise ratio were excluded from processing, and as a result, the winds below 6 m/s were biased high and there were data gaps in regions of low winds. Finally, this statistical analysis also indicated that the SASS winds were biased high by about 1 m/s.

Woiceshyn et al. [this issue] recently observed some of these same problems with the SASS-I winds. However, their conclusion that the inconsistencies in the SASS-I winds are due the inadequacy of the σ^0 power law model disagrees with the results reported herein. As we will show, the major problem is not the form of the power law model but rather the original coefficients appearing in the model. The one exception is the nadir NRCS, which does seem to deviate from a constant power law relationship. When the correct values for the coefficients are used, the off-nadir power law model yields winds that are consistent to within ± 0.5 m/s between polarizations and ± 0.2 m/s over incidence angle. These residual systematic errors are much smaller than the errors in the SASS-I winds.

To evaluate the SMMR winds, Wentz et al. [1982] compared SMMR winds from 11 orbit segments over the North Pacific and North Atlantic with collocated SASS winds. In addition, a small number of the SMMR winds were directly compared with high-quality buoy spot observations. At the time, the SASS winds had already undergone a relatively thorough investigation via JASIN and GOASEX, and it was more expedient to compare the SMMR winds with the SASS winds than to repeat the in situ field analyses for SMMR. The SMMR and SASS winds were easily compared because their swaths overlapped. A least squares algorithm for SMMR was first tuned to the SASS winds for two orbit segments over the North Pacific, and then comparisons were made for the other orbit segments. These SMMR/SASS comparisons showed 1.4-m/s agreement with no bias. This good agreement for the SMMR/SASS comparisons indicated a high correlation exists between the types of roughness sensed by the two instruments. The limited number of SMMR versus in situ comparisons gave a 1.8-m/s variation with a 0.7-m/s bias.

For the original production of the 3-month SMMR geophysical data set, a simple regression algorithm was used [Cardone et al., 1983], rather than the least squares algorithm mentioned above. With respect to wind speed, the regression algorithm had a serious flaw. An 'ad hoc' sea-surface temperature term was added to the wind regression to make the SMMR winds agree with the SASS winds for a few observations in the tropics. Later, when analyzing the SMMR global winds on a monthly basis, D. Chelton (private communication, 1983) discovered an artificial correlation between the SMMR wind and sea-surface temperature. This false correlation was due to the ad hoc term. The SMMR winds were also falsely correlated with the atmospheric liquid water content. These and other problems with the regression algorithm are described by Wentz et al. [1981]. In addition to the algorithm problems, the SMMR brightness temperatures (T_B) suffered from absolute biases, temporal drifts, and systematic errors that depended on the swath position [Bernstein and Morris, 1983].

In view of the above problems with the original SASS and SMMR winds, we have reprocessed the SASS and SMMR sensor data. As is discussed herein, the wind retrieval algorithms are deterministic inversion routines, which are much simpler than the least squares methods used in the past. The algorithms are based on NRCS and T_B models that are derived without using in situ anemometer measurements. The only assumption concerning wind speed is that the winds observed by SASS were Rayeigh distributed about a mean value of 7.4 m/s [Wentz et al., 1984]. Thus the new SASS and SMMR winds are completely independent of any particular set of conventional observations.

This statistical derivation has a distinct advantage over the usual approach of 'tuning' the algorithm to the in situ observations. It fully utilizes the large number of observations collected by satellite sensors. In contrast, the amount of good quality in situ observations is very limited. Even the highest quality JASIN winds had errors. An additional problem with using in situ data for model and algorithm development is the mismatch between the spatial and temporal scales of the satellite footprint and the in situ point observation. In other words, there are simply not enough in situ data of sufficient accuracy to specify the many degrees of freedom exhibited by σ^0 and T_B. The systematic errors in the JASIN-derived SASS-I algorithm and the SMMR regression algorithm attest to this.

A final comment should be made concerning the measurement of surface roughness as opposed to wind speed. The radiometer and scatterometer directly respond to variations in surface roughness, not wind speed. Variations in the atmospheric stratification will degrade the correlation between surface roughness and wind speed measured at some height. Furthermore, it is likely that some other atmospheric parameter or combination of parameters will correlate better with the roughness than wind speed. Thus the wind speed coming from the algorithms presented herein is more indicative of a roughness index than an actual wind speed. The high correlation that is obtained between the SMMR and SASS wind speeds indicates the types of roughness sensed by the two instruments (wave tilting and white-capping for SMMR and capillary waves for SASS) are highly correlated. It does not indicate that the surface roughness is correlated with wind speed. To examine the roughness versus wind correlation, one must refer to the in situ comparisons.

In this paper, we first discuss the format for

the various wind comparisons to be shown. Then we describe the new SASS NRCS model and wind retrieval algorithm. The SASS winds are compared with 1623 National Data Buoy Office (NDBO) buoy observations. Next, the development of the SMMR T_B model and geophysical algorithm is described. The SMMR and SASS winds are then compared on a 150-km cell-by-cell basis over the Seasat 3-month period from July to October 1978. We conclude by discussing the upcoming satellite radiometer system SSM/I.

Wind Comparison Figures

Throughout this paper, we compare pairs of different wind speed estimates. In particular, the following comparisons are made.

1. SASS off-nadir winds versus SASS nadir winds.
2. SASS h-pol winds versus SASS v-pol winds.
3. Winds from adjacent SASS cells.
4. SASS winds versus in situ buoy winds.
5. SASS winds versus SMMR winds.

The usual method of illustrating the wind speed comparisons is to plot one wind estimate versus the other in the form of a scatter plot. However, in this investigation we typically have tens of thousands of wind pairs to plot, and a scatter plot would appear as a large solid area, giving little information about the relevant statistics. Thus we choose an alternative method for plotting the data. The wind speed pairs are first stratified into 1-m/s wind speed bins, and the variation of data points in each bin is computed. Then we plot the ±1 standard deviation contours for the collection of bins.

When binning the data, the spatial and temporal mismatch between the two wind observations must be considered, particularly for cases involving extremely high or low winds. Because of the mesoscale variability in the wind field, two different wind speeds will be observed. For example, consider two locations on the ocean, and let the observed winds be denoted by W_1 and W_2. Futhermore, note that the probability of observing an extreme wind speed, either high or low, is less than the probability of observing a moderate wind speed. Thus if W_1 is observed to be zero, the likelihood is that W_2 will be somewhat greater than zero. Likewise, when W_1 is observed to be extremely high, W_2 will, on the average, be less. Now assume that the W_1 and W_2 pairs were binned according to W_1. Thus for the low wind speed bins, W_2 would be greater than W_1, and for the high wind speed winds W_2 would be less. In presenting the data, this type of biasing is undesirable. A better way to present the data is to plot the difference between W_1 and W_2 versus the average of W_1 and W_2. In this way the statistics are symmetrical, and for a given bin, W_1 should equal W_2 on the average. In other words, when the wind pairs are binned according to their average, no preference is given to W_1 or W_2.

For the wind plots in this paper, the abscissa always corresponds to the average $\bar{W}$ of the two wind estimates, and the ordinate corresponds to the difference ΔW between the two estimates. The wind pairs are stratified into 1-m/s bins according to $\bar{W}$. All wind pairs falling in a given bin are averaged to find the mean values $\langle \bar{W} \rangle$ and $\langle \Delta W \rangle$. In addition the standard deviation of ΔW, $SD(\Delta W)$, is found. The mean and ±1 standard deviation points for a given bin are then defined by $(\langle \bar{W} \rangle, \langle \Delta W \rangle)$, $(\langle \bar{W} \rangle, \langle \Delta W \rangle + SD(\Delta W))$, and $(\langle \bar{W} \rangle, \langle \Delta W \rangle - SD(\Delta W))$, respectively. The respective points for adjacent bins are connected by straight lines, thereby constructing a mean curve and a ±1 standard deviation envelope.

SASS NRCS Model

The SASS normalized radar cross-section (NRCS or σ^0) model expresses σ^0 in terms of wind speed and direction, incidence angle, and polarization. We use the model developed by Wentz et al. [1984] with a few modifications. This model expresses the NRCS as

$$\sigma^0 = A_0 + A_1 \cos(\omega - \omega_w) + A_2 \cos[2(\omega - \omega_w)] \quad (1)$$

The angles ω_w and ω are azimuth angles for the wind direction and σ^0 measurement, respectively. The A coefficients are functions of the polarization, incidence angle, and wind speed W. The coefficients A_0 and A_2 are derived from a statistical analysis of the 3 months of SASS σ^0 observations, in which no in situ anemometer measurements are used. This statistical derivation is designed to preclude, as much as possible, systematic errors in the σ^0 versus polarization and incidence angle relationship. The A_1 coefficient comes from the Advanced Applications Flight Experiment radiometer-scatterometer (AAFE RADSCAT) aircraft circle measurements of σ^0 [Jones and Schroeder, 1978].

Three changes are made to the original Wentz et al. [1984] model. The first change involves the nadir NRCS and is relatively important, while the other two changes are minor. The original model assumed that the nadir σ^0 could be characterized by the same type of constant power law relationship as was used for the off-nadir σ^0, i.e.,

$$A_0 = a_0 W^{\alpha_0} \quad (2)$$

(At nadir there is no wind direction dependence, and the A_1 and A_2 coefficients are zero.) However, when the nadir winds are compared with the neighboring off-nadir winds, a significant systematic error occurs. Figure 1 shows the nadir winds compared with the wind from the first off-nadir cell, which has an incidence angle of about 24°. The comparisons are for the 3 months of v-pol SASS data, which represent 340,000 wind pairs. The algorithm for computing the winds is described below. The nadir and off-nadir cells are separated by about 250 km. The solid curve shows the mean difference between the off-nadir wind minus the nadir for the port side of the SASS swath. The dashed curve shows the results for the starboard side. The port and starboard sides show nearly the same systematic error in the wind retrievals. A similar plot of the winds computed from the h-pol σ^0's shows the same error signature. As is discussed below, the power law relation (2) gives very consistent results when comparing the winds from all of the adjacent off-nadir cells. Thus we attribute the error shown in Figure 1 to the assumed power law relationship for the nadir σ^0. To correct the error, a more general relationship must be used.

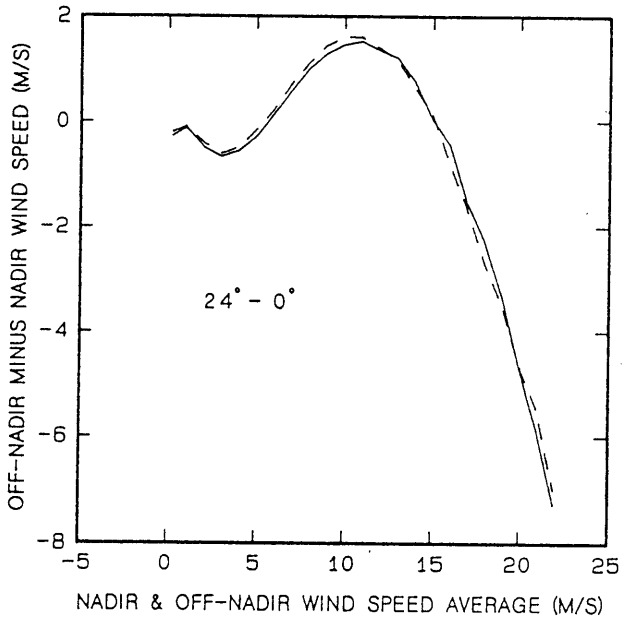

Fig. 1. A comparison of SASS nadir winds and off-nadir winds assuming a power law relationship for the nadir NRCS. The solid (dashed) curve shows the results for the port side (starboard) winds.

Rather than specifying a functional form for the nadir σ^0 versus wind relationship, we compute Table 1 that gives σ^0 in decibels for winds ranging from 0.5 to 30 m/s in 0.5-m/s steps. The derivation of Table 1 is an iterative procedure that removes the error signature shown in Figure 1. Figure 2 shows the resulting table values connected by linear segments. A logarithm scale is used for wind speed in order to show the departure of the table values from a power law relationship, which would be a straight line in Figure 2. For winds below 15 m/s, the σ^0 versus wind relationship is very similar to that found in the Seasat altimeter analysis by Chelton and McCabe [1985], who assumed a power law relationship. For winds above 15 m/s, our σ^0's fall off faster with increasing wind speed than does the Chelton-McCabe curve. This may be due to the sparsity of high-wind data points in the Chelton-McCabe analysis.

The second change involves the wind speed dependence of the ratios A_1/A_0 and A_2/A_0. The assumed wind dependence in the original model was

$$A_j/A_0 = a_j + \alpha_j \ln W \qquad (3)$$

where $j = 1$ or 2 and W is wind speed (in meters per second). For low winds near 1 m/s and high incidence angles near 60°, the ratios given by (3) exceed unity, and as a result the σ^0 given by (1) is less than zero for cross-wind observations, which is unphysical. To prevent this, the following linear spline to (3) is used for W less than 8.155 m/s:

$$A_j/A_0 = a_j + \alpha_j (\ln 3 + W/8.155) \qquad (4)$$

which is continuous in the zeroth and first derivatives of W. The spline point of 8.155 m/s is chosen so that the value of (4) at $W=0$ equals the

TABLE 1. Nadir NRCS at 14.6 GHz Versus Wind Speed

Wind Speed, m/s	NRCS, dB
0.5	18.45
1.0	15.45
1.5	14.62
2.0	13.94
2.5	13.48
3.0	13.13
3.5	12.83
4.0	12.58
4.5	12.37
5.0	12.18
5.5	12.01
6.0	11.86
6.5	11.72
7.0	11.58
7.5	11.45
8.0	11.33
8.5	11.21
9.0	11.09
9.5	10.97
10.0	10.85
10.5	10.73
11.0	10.61
11.5	10.49
12.0	10.37
12.5	10.24
13.0	10.12
13.5	9.99
14.0	9.85
14.5	9.71
15.0	9.57
15.5	9.43
16.0	9.28
16.5	9.13
17.0	8.98
17.5	8.82
18.0	8.66
18.5	8.51
19.0	8.35
19.5	8.19
20.0	8.03
20.5	7.87
21.0	7.72
21.5	7.56
22.0	7.40
22.5	7.24
23.0	7.08
23.5	6.93
24.0	6.77
24.5	6.61
25.0	6.45
25.5	6.30
26.0	6.14
26.5	5.98
27.0	5.82
27.5	5.66
28.0	5.51
28.5	5.35
29.0	5.19
29.5	5.03
30.0	4.88

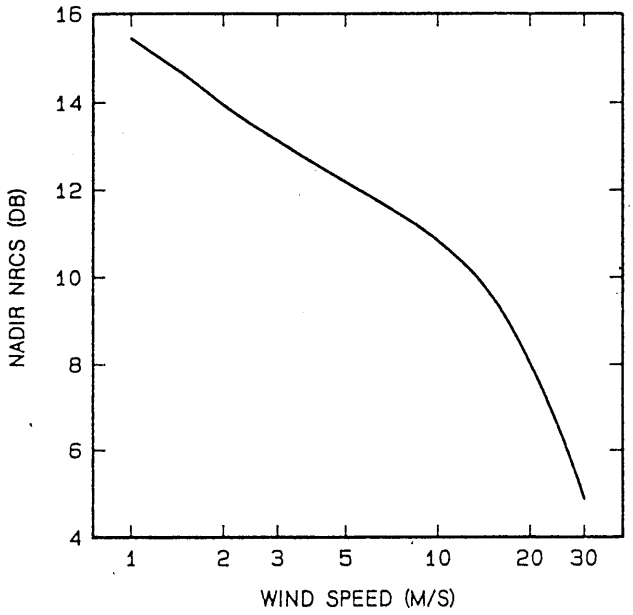

Fig. 2. The relationship between the nadir NRCS and wind speed as derived from a comparison of nadir and off-nadir SASS winds.

value of (3) at W=3. In this way, the value of the ratio given by (4) for low winds is about the same as was given by (3). For winds greater than 20 m/s, the wind dependence is also modified. This change is mostly cosmetic because winds above 20 m/s are rare. The high wind speed spline is

$$A_j/A_0 = a_j + \alpha_j [\ln W - (W-20)^2/600] \qquad (5)$$

When W equals 30 m/s, the derivative of (5) with respect to wind speed is zero. For winds greater than 30 m/s, the ratios are assumed constant and are equal to the 30 m/s value given by (5).

The third change to the model involves modifying the 10 m/s value of the A_0 coefficients. The winds coming from the original model show systematic errors of the order of 0.5 m/s or less that can be directly attributed to a misspecification of the A_0 coefficients. These errors are easily eliminated by slightly modifying the A_0 coefficients. The required changes in the 10-m/s A_0 coefficients are only about 0.1 to 0.2 dB. Note that small systematic errors remain in the SASS winds, as is discussed below. These errors can not be corrected by simply modifying A_0.

SASS Wind Retrieval Algorithm

The SASS wind retrieval algorithm computes wind speed at a 100-km resolution. Wind direction is also computed but is not considered herein. The first step is to average the σ^0 measurements that fall within a 100-km-square cell. The 100-km cells are formed by a rectilinear grid system having an x axis aligned to the satellite subtrack and a y axis perpendicular to the subtrack. For one complete orbit, there are exactly 410 cells in the subtrack direction and 15 cells in the cross-track direction. The eighth cross-track cell is the nadir cell that is bisected by the subtrack. The nadir σ^0 observations are averaged together irrespective of polarization or antenna. (However, v-pol measurements from antenna 3 are not used because of a very low antenna gain.) The off-nadir σ^0 observations are averaged separately according to the polarization and antenna.

The preaveraging of σ^0 before retrieving wind speed increases the signal-to-noise ratio (snr). A 100-km cell in the middle of the SASS primary swath typically contains four observations from each antenna. Averaging these observations increases the snr by a factor of 2. For light winds below 6 m/s, the snr is poor, and the preaveraging helps considerably. In the SASS-I algorithm no preaveraging was done. The low snr measurements were simply excluded from processing, which resulted in data gaps in low wind speed areas and a positive bias in the retrieved wind speeds for moderate wind speed areas. In the new algorithm, all σ^0 measurements are used, regardless of the snr value. Sometimes under light wind conditions, a σ^0 measurement is less than zero due to the measured signal plus noise being less than the measured noise. These negative σ^0's are also included in the averaging. In this way, the retrieved low winds are free of the positive bias that occurred in the original processing.

For nadir observations, the wind speed is found by linearly interpolating Table 1 to the averaged σ^0 measurement. A minor adjustment is made to account for the incidence angle not being exactly zero. (For the SASS nadir cell the incidence angle ranges from 0° to about 1°.) For off-nadir observations, the averaged σ^0 measurements for two orthogonal antennas must be combined in order to remove the wind direction effect. We require that the two orthogonal measurements be the same polarization. The pair of averaged orthogonal measurements is represented by

$$\langle\sigma^0\rangle_i = \langle A_0\rangle_i + \langle A_1\rangle_i \cos(\omega_i-\omega_W) + \langle A_2\rangle_i \cos[2(\omega_i-\omega_W)] \qquad (6)$$

where subscript i denotes the antenna (i = 1 or 2) and $\langle\cdots\rangle_i$ denotes an average over the 100-km cell. Note that within a 100-km cell, the σ^0 azimuth angles ω_i are essentially the same, and we have assumed that the wind direction ω_W is constant over the cell. Thus terms involving these angles can be removed from the averages.

Equation (6) represents two equations in two unknowns, W and ω_W. The equations are solved by noting that the azimuth angles ω_1 and ω_2 are orthogonal ($\omega_2 = \omega_1 + 90° \pm 1°$). Using this orthogonality property, the second harmonic in the two equations is eliminated, giving

$$\langle A_2\rangle_2 \langle\sigma^0\rangle_1 + \langle A_2\rangle_1 \langle\sigma^0\rangle_2 = \langle A_2\rangle_2 \langle A_0\rangle_1 + \langle A_2\rangle_1 \langle A_0\rangle_2 + \varepsilon \qquad (7)$$

$$\varepsilon = \langle A_2\rangle_2 \langle A_1\rangle_1 \cos(\omega_1-\omega_W) - \langle A_2\rangle_1 \langle A_1\rangle_2 \sin(\omega_1-\omega_W) \qquad (8)$$

The term ε arises because there is a difference between an upwind and a downwind measurement of σ^0. If the upwind and downwind σ^0 were equal, then A_1 would be zero. As is discussed in the next paragraph, the best estimate of wind speed is found by setting ε to zero, which gives

$$F(W) = \langle A_2 \rangle_2 \langle \sigma^0 \rangle_1 + \langle A_2 \rangle_1 \langle \sigma^0 \rangle_2 - \langle A_2 \rangle_2 \langle A_0 \rangle_1 - \langle A_2 \rangle_1 \langle A_0 \rangle_2 = 0 \quad (9)$$

The only unknown in the function F(W) is wind speed W, which is found by Newton's iterative method. Only two or three iterations are required for convergence. The wind speed error introduced by neglecting ε is approximately

$$\Delta W = -\varepsilon / [\partial F(W)/\partial W] \quad (10)$$

The percentage error $\Delta W/W$ is typically about 6% and 2% for h-pol and v-pol, respectively.

The first and second harmonics in (6) produce multiple solutions for ω_w, which are called wind direction ambiguities. The number of these ambiguities is between 0 (no solution) and 4. Each ambiguity has a slightly different wind speed solution because of the upwind-downwind term ε. Although the term ε is different for each ambiguity, its average over the various ambiguities is nearly zero. Thus setting ε to zero in the above analysis is equivalent to taking the average of the wind speeds associated with the ambiguities. This procedure gives the best estimate of wind speed that can be obtained if there is no additional information on wind direction, which is the case for this investigation.

The 3-month SASS data set is processed through the algorithm, and winds are found for 2 million 100-km cells. The wind speeds are analyzed to reveal any systematic errors in polarization and incidence angle. Figures 3 through 5 show the results of this analysis. In the figures, the results for the SASS port cells are shown by solid lines, and the dashed lines show the results for the starboard cells.

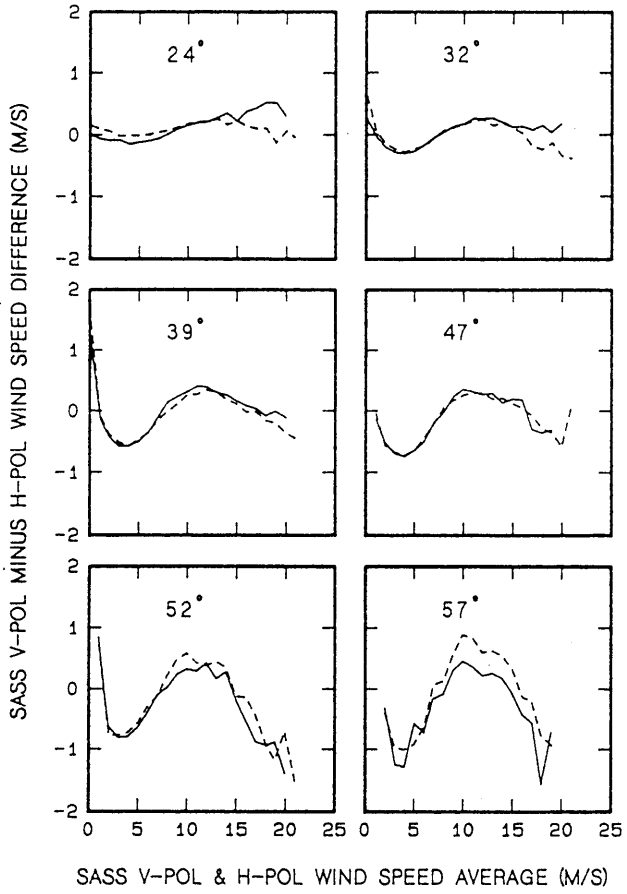

Fig. 3. A comparison of SASS winds derived from h-pol observations with those derived from v-pol observations. The solid (dashed) curve shows the results for the port side (starboard) winds. Six different incidence angle cells are shown.

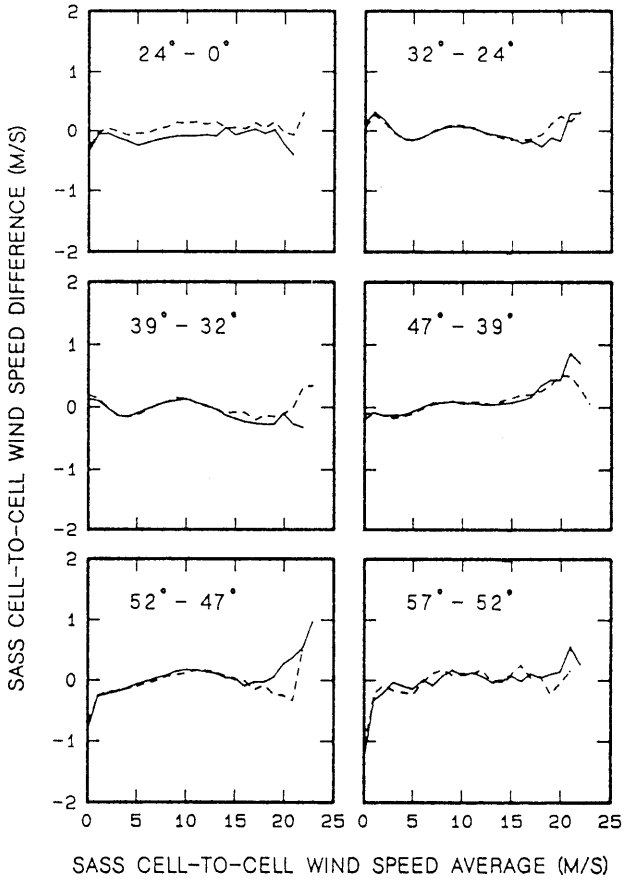

Fig. 4. A comparison of SASS winds from adjacent incidence angle cells derived from v-pol observations. The solid (dashed) curve shows the results for the port side (starboard) winds.

Figure 3 compares the winds computed from the h-pol σ^0's with those computed from the v-pol σ^0's. These comparisons are done for the six off-nadir cells, which have average incidence angles of 24°, 32°, 39°, 47°, 52°, and 57°, respectively. We only use those cells that have both h-pol and v-pol σ^0's (i.e., SASS modes 3 and 4). The plots show the difference of the v-pol wind minus the h-pol wind plotted versus the average of the v-pol and h-pol wind. For each incidence angle there are about 30,000 v-pol/h-pol wind pairs, except for the 57° cell, which has about 6,000 pairs. There is a definite, though small, systematic difference between the v-pol and h-pol winds at the higher incidence angles. Both the port and starboard winds show the same error signature. The magnitude of this error is about ± 0.5 m/s, and for most applications will be of little consequence. However, its occurrence is very interesting, and we do not yet have an explanation for it. The v-pol and h-pol winds from the nadir cell are also compared, and, as expected, show no significant difference.

Figures 4 and 5 compare the winds from adjacent cells across the SASS swath for v-pol and h-pol, respectively. On each side of the swath, there are six sets of adjacent cells. The first set consists of the nadir cell and the first off-nadir cell having an average incidence angle of 24°. The separation between these two cells is about 250 km. For the other five sets, the separation between adjacent cells is only 100 km. For v-pol, there are about 340,000 wind pairs for each adjacent cell set, except for the last set consisting of the 52° and 57° cells, which has about 30,000 wind pairs. For h-pol there are fewer observations. Typically, there are 40,000 wind pairs for each adjacent cell set, except for the last set, which has about 7,000 pairs. These figures plot the wind speed difference of the higher incidence angle wind minus the lower incidence angle wind versus the average of the two wind speeds. The v-pol comparisons show very small systematic errors of the order of 0.2 m/s. For example, in the 32° minus 24° wind comparisons, the port and starboard curves coincide to better than 0.1 m/s and show an error signature having an amplitude of 0.2 m/s. The cause of these small errors is unknown. The extremely close agreement between data taken from the port and starboard sides indicates that the sample size is sufficiently large to effectively filter out the effect of wind gradients over the pair of adjacent cells. It also shows the precision that can be obtained by using large global data sets to remove systematic errors in the wind retrievals.

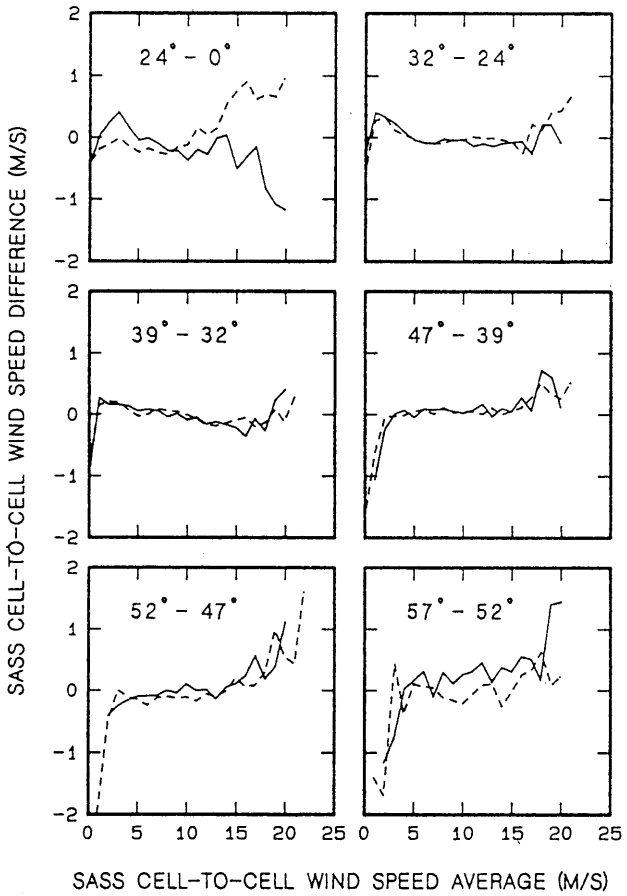

Fig. 5. A comparison of SASS winds from adjacent incidence angle cells derived from h-pol observations. The solid (dashed) curve shows the results for the port side (starboard) winds.

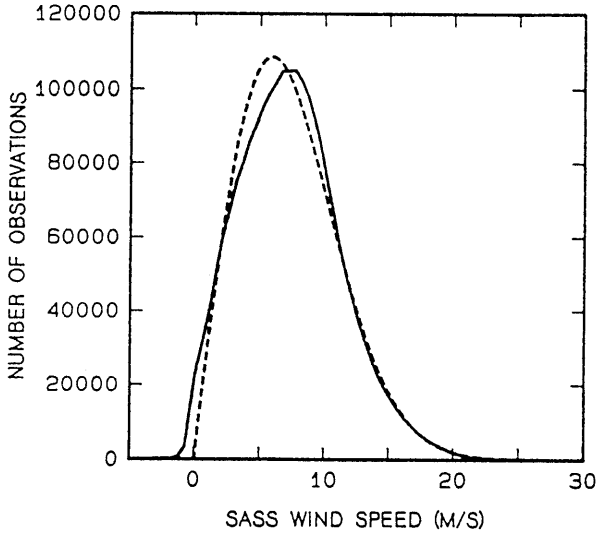

Fig. 6. A comparison of the histogram of SASS winds (solid curve) with a Rayleigh distribution having a 7.4 mean wind speed (dashed curve).

The h-pol curves in Figure 5 are a little more noisy than the v-pol curves because of the smaller number of samples. Also, the results for wind speeds near zero show considerable scatter due to the very low snr that occurs for low-wind h-pol observations. For winds below 3 m/s, there seems to be a trend for the higher incidence angle cell to retrieve a lower wind speed. This is probably caused by a small error in the volt-to-σ^0 algorithm. The effect of such an error is magnified when the snr is low.

As mentioned above, the derivation of the SASS σ^0 model assumes that the wind speeds observed by SASS during its 3 months in operation were distributed as a Rayleigh probability density function (pdf). A Rayleigh distribution has only one degree of freedom, which can be expressed in terms of its mean. This mean wind speed was set to 7.4 m/s based on climatology. No other assumptions concerning wind speed were made, and no in situ observations were used in the derivation. To show that the Rayleigh assumption is self-consistent, we conclude this section by presenting Figure 6, which is a histogram of 2,115,041 SASS winds for the 3-month period. The solid line in Figure 6 is the SASS wind histogram that was constructed from 0.5-m/s bins. The mean and standard deviation of these winds are 7.4 and 3.9 m/s, respectively. The dashed line shows a Rayleigh distribution having the same 7.4-m/s mean. As can be seen, the distribution of SASS winds is very close to Rayleigh.

SASS and In Situ Wind Comparisons

Since the SASS wind algorithm is derived without using in situ data, two important questions arise. The first concerns the validity of the statistical assumptions used in the derivation, i.e., the Rayleigh distribution of winds. The second concerns the degree of correlation that

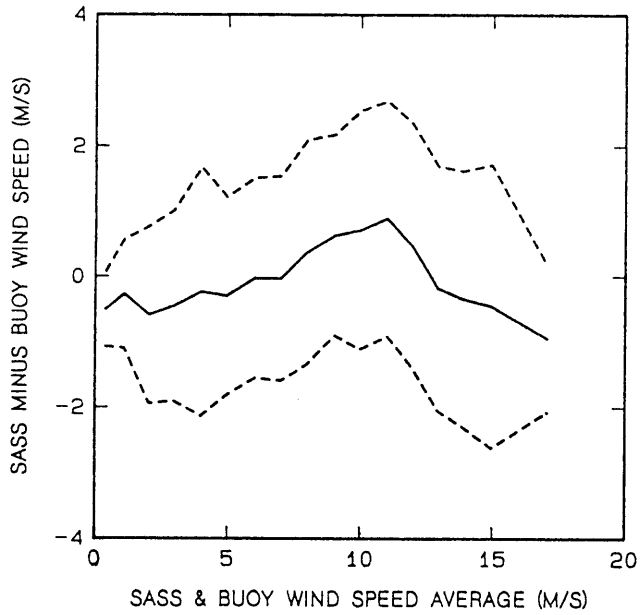

Fig. 7. A comparison of SASS winds with 1623 NDBO buoy observations. The solid curve shows the mean difference, and the dashed curves are the ±1 standard deviation envelope.

exists between the surface roughness sensed by SASS and the near-surface wind speed. In order to address these questions, we compare the SASS winds with 1623 NDBO buoy observations provided by Chelton and McCabe [1985]. The in situ data set is obtained from 19 buoys located off the East and West Coast of North America and in the Gulf of Mexico. The buoy winds represent an 8.5-min average that is taken hourly. For the comparisons, we use all SASS winds that lie within a 100-km radius and a ±1 hour interval of the buoy observation. The SASS winds falling within this spatial and temporal window are averaged together and then compared with the buoy wind. When averaging SASS winds, a $1/R^2$ weighting is used, where R is the distance between the buoy and the SASS cell. No distinction is made between the nadir and off-nadir SASS winds or between the SASS winds coming from h-pol and v-pol σ^0's. This selection procedure results in 1659 SASS/buoy wind pairs. Of these, 36 cases (2% of the total) are excluded because of anomalously large (>5 m/s) discrepancies between the two wind estimates. A major source of error in this type of comparison is the spatial and temporal sampling mismatch between the SASS and the buoy. This sampling error prohibits seeing the true correlation between the SASS wind and the actual wind averaged over the SASS cell at the time of the SASS overpass. This true correlation is most likely higher than that obtained from the SASS/-buoy comparisons presented below.

Figure 7 shows the difference of the SASS wind minus the buoy wind plotted versus the average of the SASS and buoy wind. The solid curve represents the mean SASS minus buoy wind difference, and the dashed curves are the ±1 standard deviation envelope. The rms discrepancy between the 1623 SASS and buoy wind pairs is 1.6 m/s, with a small -0.1 m/s overall bias. The correlation between the two wind estimates is 0.89. Figure 7 shows good agreement between the two wind estimates over the entire 0- to 17-m/s range. Considering the fact that the new SASS algorithm has never been 'tuned' to in situ observations, this close agreement with the in situ is quite remarkable and verifies the validity of the statistical assumptions used in the algorithm development. Furthermore, these results along with the earlier findings of the GOASEX and JASIN experiments indicate that there is indeed a good correlation between the SASS wind speed, which is inferred from surface roughness, and the actual near-surface wind speed over the ocean.

SMMR T_B Model

The SMMR brightness temperature (T_B) model gives the brightness temperature in terms of the relevant environmental parameters. We use the model developed by Wentz [1983a] with a few modifications. This model expresses T_B as

$$T_{Bi} = f_i(T_s, W, V, L) \qquad (11)$$

where $f_i(\cdots)$ is a relatively simple closed-form expression. The subscript i denotes the SMMR channnel. The environmental parameters are sea-surface temperature T_s (in degrees Kelvin), wind speed W (in meters per second), atmospheric columnar water vapor V (in grams per square centimeter), and atmospheric columnar liquid water L (in grams per square centimeter). Three changes are made to the Wentz [1983a] model, and we discuss them in order of importance.

The first change in the model involves the wind-induced emissivities ΔE. The original derivation of ΔE indicated that the relationship between ΔE and wind speed is nonlinear. To model this behavior, two linear segments were used, one for low winds (0 to 14 m/s) and a steeper one for high winds (>16 m/s). These segments were connected by a quadratic spline. We continue to use this general form but change the two spline points to 7 m/s and 17 m/s. These new spline points are determined from a visual inspection of the ΔE plots discussed below. It is interesting to note that the 7-m/s point corresponds to the wind speed at which foam first appears [Nordberg et al., 1971; Wilheit and Chang, 1980]. Also, we expressed ΔE in terms of wind speed rather than friction velocity, which was used in the original formulation, because the SASS algorithm is parameterized in terms of wind speed. (The original derivation simply assumed friction velocity was 0.047 times wind speed.) The wind-induced emissivity is now given by

$$\Delta E = m_1 W \qquad W \leq 7 \qquad (12a)$$

$$\Delta E = m_1 W + 0.05(m_2 - m_1)(W-7)^2 \qquad 7 < W < 17 \qquad (12b)$$

$$\Delta E = m_2 W - 12(m_2 - m_1) \qquad W \geq 17 \qquad (12c)$$

As is discussed below, the coefficients m_1 and m_2 are rederived using the entire 3 months of SMMR brightness temperatures collocated with SASS wind speeds. In the Wentz [1983a] derivation, the m's were based on data from just two Seasat orbit segments over the North Pacific, which consisted of only 119 SMMR cells. Furthermore, the original derivation used the SASS-I winds that suf-

fered from the above-mentioned systematic errors. Thus we place much more confidence in the new m's than the old.

The second change to the T_B model is to modify the atmospheric absorption coefficients at 37 GHz. In the original model, the Rayleigh scattering approximation was used to specify the liquid water absorption coefficient at 37 GHz. The absorption coefficients at the lower frequencies were then adjusted relative to the 37-GHz Rayleigh value. The adjustments were primarily designed to obtain consistency between the liquid water retrievals coming from the 18-GHz channels and those coming from the 37-GHz channels. In retrospect, it is more logical to use Rayleigh absorption coefficients for the lower frequencies and then to modify the 37-GHz coefficient. The Rayleigh approximation assumes that the ratio between the water droplet radius and the radiation wavelength is much less than unity, and thus is more valid at the lower frequencies. In the new model the unmodified Rayleigh values are used for the 6.6- through 21-GHz channels. At 37 GHz, the Rayleigh value is reduced as is discussed below. Likewise, the water vapor absorption coefficient at 37 GHz is also reduced in order to obtain consistent liquid water retrievals for high water vapor contents.

The third change affects the air temperature T_a dependence in the model. This change is of minor importance, and its primary purpose is to simplify the model. The dependence of T_B on T_a is quite weak for nonraining cases. The layer of atmosphere that is responsible for the observed brightness temperatures extends from the surface up to about 5 km. A nominal value of 265 K is assumed for the air temperature at the top of the layer, and the air temperature at the surface is assumed equal to the surface temperature T_s. The average temperature of the layer is then

$$T_a = (T_s + 265)/2 \qquad (13)$$

In the original model, T_a was assumed to decrease linearly with altitude h according to the lapse rate λ. We now use (13) to specify a single air temperature for the atmosphere. This change has a very small effect on the computed brightness temperature except for highly attenuating atmospheres for which unmodeled rain effects are the dominant source of error. The other change to the T_a dependence is to set the temperature sensitivities for the liquid water absorption coefficients to zero. Since there is a high degree of uncertainty in the temperature profile of the cloud water, a temperature correction for the liquid water absorption is not warranted.

SMMR T_B Biases and Model Coefficients

A systematic procedure is used to find the biases in the SMMR T_B's, the wind-induced emissivity coefficients, and the 37-GHz atmospheric absorption coefficients. In this procedure, the newly generated SASS winds are used to determine the wind-induced emissivity coefficients in the T_B model. However, the SASS winds are more of a convenience than a necessity. The wind dependence in the T_B model could have been determined independent of SASS via the same statistical approach used by Wentz et al. [1984] to determine the σ^0 model wind dependence. This was done in an alternative derivation, and the results were essentially the same as reported below. The procedure only uses the SMMR grid 1 brightness temperatures, which are averaged onto 150-km-square cells that are aligned to the satellite subtrack. There are four such cells across the SMMR's 600-km-wide swath. Njoku et al. [1980a] describes this gridding system in detail. Only those cells that are at least 800 km away from land are used in order to avoid antenna sidelobe contamination at the lower frequency channels.

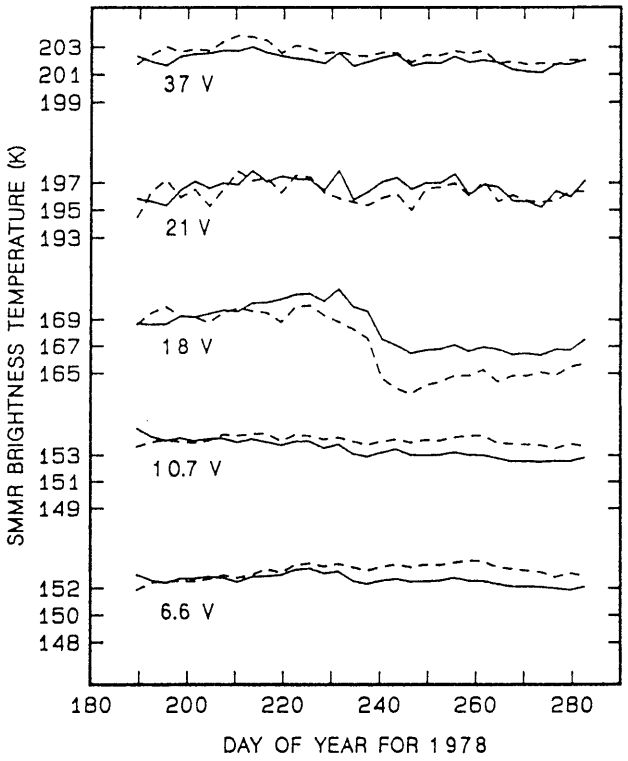

Fig. 8. A time history of the ocean brightness temperatures for the five SMMR v-pol channels. The solid (dashed) curves show the results for the descending, nighttime (ascending, daytime) orbit segments.

Before describing the procedure for the bias removal and coefficient determination, we first give an overview of the SMMR T_B bias problem. Figure 8 shows global, 3-day averages of the T_B measurements in the open ocean. The average T_B's for the five SMMR v-pol channels are plotted versus time. The channel frequencies are 6.6, 10.7, 18, 21, and 37 GHz. The solid curve is for the descending portion of the orbit, and the dashed curve is for the ascending portion. For Seasat, the descending orbit segment occurred in the evening, and the ascending orbit segment occurred in the morning. The most striking feature in Figure 8 is the sudden 5 K drop in the level of the 18-GHz channel that occurs near day 239 (August 27). A similar plot of the h-pol channels shows the same anomaly for 18 GHz. None of the other channels shows this behavior, and we attribute it to a sensor malfunction rather than a geophysical signal. Possibly the transmission characteristics of a ferrite switch may have degraded. Another indication of a faulty front-

end waveguide component is the large separation between the 18V T_B for ascending orbit segments as compared to the descending orbit segments. If one of the transmission coefficients in the volts-to-antenna temperature transfer function were to change, then the transfer function would not correctly compensate for the change in the SMMR internal temperature as the spacecraft goes from day to night. Note that the 6.6V and 10.7V T_B's are somewhat higher for the daytime orbit segments. This effect is the opposite of that for the 18V T_B and is attributed to sea-surface sun glitter. Because Seasat was not in a sun-synchronous orbit, the sun glitter contamination was significant only during the second half the mission.

The SMMR T_B biases, the wind-induced emissivity coefficients, and the 37-GHz absorption coefficients are found from the following four-step procedure.

1. T_B biases in the 21V and 37V channels are found from comparisons with radiosonde water vapors and from a histogram of liquid water contents.

2. The T_B bias in the 18V channel is found, and the atmospheric absorption coefficients at 37 GHz are modified. This is done by comparing the liquid water contents retrieved from the 37V and 21V channels with those retrieved from the 18V and 21V channels.

3. The wind-induced emissivity coefficients for 18V, 21V, and 37V are modified based on the assumption of zero correlation between wind speed and liquid water.

4. T_B biases and wind-induced emissivity coefficients for the remaining seven channels are found.

Steps 1, 2, and 3 are iterated as a group four times until the biases and coefficients being determined reach stable values (0.1 K in the T_B biases and 1% in the parameters). Then step 4 is iterated three times to obtain stable values for the remaining biases and coefficients.

In step 1, a two-channel retrieval algorithm is used to find the columnar water vapor V and columnar liquid water L, given the 21V and 37V T_B's. This algorithm requires that the parameters T_s and W be specified. Note that the 21V and 37V T_B's are relatively insensitive to T_s and W. Reynolds' [1982] climatology is used to specify T_s, as discussed below. The newly generated SASS winds are used to specify W. All SASS winds that have cell centers within a 200-km radius of the SMMR cell center are averaged together. When averaging SASS winds, a $1/R^2$ weighting is used, where R is the distance between the SASS and the SMMR cell. To find V and L, the algorithm inverts the two equations represented by (11), with subscript i denoting 21V and 37V. Although the function f_i is nonlinear in V and L, it does increase monotonically with V and L. Hence the two equations are easily inverted using Newton's method extended to two dimensions. The details of this type of inversion are given below.

The retrieved vapors are compared with radiosonde observations. Alishouse [1983] assembled a collection of radiosonde flights from 10 stations in the North and Tropical Pacific. When comparing the SMMR and radiosonde vapors, the SMMR cell is required to be within a 100-km radius of the radiosonde station. This procedure yields 91 comparisons with the radiosondes. The mean difference ΔV between the SMMR and radiosonde water vapor is then calculated. In addition to the water vapor comparisons, a histogram of 258,396 retrieved liquid water contents is constructed from the 3-month SMMR data set. Ideally, the left side of the histogram should be zero for $L<0$ and should abruptly increase at $L=0$, which corresponds to clear sky conditions. However, noise in the L retrievals broadens the histogram and causes negative L values to occur. Assuming the noise is zero-mean Gaussian and the left side of the true histogram is a step function, then the point at which the noisy histogram drops to one half its maximum value should correspond to $L=0$. We use this left-side midpoint as an indicator of the bias in the liquid water retrievals. The distance that this midpoint is offset from zero is denoted by ΔL.

For the first iteration, the T_B's are not corrected for biases, and the mean difference ΔV between SMMR minus radiosonde water vapors is -0.3 g/cm^2. Furthermore, the liquid water bias ΔL is -14 mg/cm^2. The T_B biases are then computed from the partial derivatives of the T_B model.

$$\Delta T_{Bi} = (\partial f_i/\partial V)\Delta V + (\partial f_i/\partial L)\Delta L \qquad (14)$$

This bias is to be subtracted from the T_B measurement to obtain the correct T_B. Note that for first iteration of steps 1 and 2, the wind-induced emissivity coefficients for 18V, 21V, and 37V are set equal to the Wentz [1983a] values, the 37-GHz liquid water absorption coefficient is set equal to the Rayleigh value, and the water vapor absorption coefficient is set equal to the Barrett and Chung [1962] value. For subsequent iterations, the coefficients found in steps 2 and 3 are used.

In step 2 we find the bias for the 18V T_B and the water vapor and liquid water absorption coefficients at 37 GHz. This step requires simultaneous measurements of the 18V, 21V, and 37V T_B's, and hence only the first 27 days of SMMR data are used in this step in order to avoid the 18-GHz anomaly mentioned above. Two sets of V and L retrievals are done, one using the 18V and 21V channels (V_1 and L_1) and the other using the 37V and 21V channels (V_2 and L_2). The biases found in step 1 are applied to the 21V and 37V channels, but no bias is applied to the 18V channel. For the first iteration, a least squares fit of L_1 versus L_2 shows a slope of about 1.2 and an ordinate intercept at $L_1=-70$ mg/cm^2. The slope should, of course, be unity, and the intercept should be at $L_1=0$. We attribute the 1.2 slope to an inadequacy in the T_B model and the nonzero intercept to a T_B bias in the 18V channel. The most obvious modification to the T_B model that will correct the slope problem is either to increase the 18-GHz coefficient or to decrease the 37-GHz Rayleigh absorption coefficient. (Note that the retrieved value of L is inversely proportional to the absorption coefficient.) We choose to decrease the 37-GHz coefficient for the reasons given above. The intercept is brought to zero by applying a bias correction to the 18V T_B. After these corrections are applied, the difference of L_2-L_1 is plotted versus V_2, and another, relatively small

systematic error is found. As the vapor content increases, L_2-L_1 decreases. This systematic error can be corrected by either increasing the 18-GHz coefficient or reducing the Barrett and Chung [1962] water vapor absorption coefficient at 37 GHz. We choose to decrease the 37-GHz coefficient. In this way, we modify only the 37-GHz absorption coefficients (both liquid and vapor), and the lower frequencies remain unaltered.

The final value that is found for the 37-GHz liquid water absorption coefficient is 1.63 napers cm^2/g, compared with 2.22 napers cm^2/g for the Rayleigh value. The 37-GHz water vapor coefficient is found to be 0.021 napers cm^2/g, which is a little less than the 0.024 napers cm^2/g value computed from the Barrett and Chung expression. It is not clear why these coefficients needed to be reduced. One possible explanation is that the 37-GHz T_B model increases too fast with L because it neglects Mie scattering from the water droplets. Another possible cause is rain cells that are small compared with the SMMR 150-km cell. Also, the temperature profile of liquid water and water vapor becomes important for highly attenuating atmospheres. An investigation using the higher resolution SMMR data would shed more light on this problem.

In the third step the wind-induced emissivity coefficients m_1 and m_2 are found for 18V, 21V, and 37V, using the 37-GHz absorption coefficients and T_B bias corrections coming from steps 1 and 2. In order to separate the wind dependence from the liquid water dependence, an assumption must be made about the W versus L correlation that exists in nature. In storms, this correlation is usually positive with high winds being associated with rain. However, for clear skies and light clouds, we assume that there is no significant correlation between W and L for the global 3-month SMMR data set. This assumption is equivalent to that made by Wentz [1983a], in which the liquid water content was set to zero for a collection of SMMR cells having low L values. Setting L to zero forces the W versus L correlation to be zero. In determining m_1 and m_2, we only use SMMR cells for which L is less than 5 mg/cm^2, which is about half of the total cells. For this subset, the coefficients m_1 and m_2 for 18V (37V) are adjusted so as to obtain a zero correlation between the SMMR liquid water retrieval L_1 (L_2) and the SASS wind speed. Note that the 21V m's are found from a linear interpolation in frequency of the 18V m's and the 37V m's. The 21V m's are not found directly because the strong water vapor signal at this frequency tends to mask the wind signal. The final values for m_1 and m_2 are given below.

The fourth and final step is to find the wind-induced emissivity coefficients m_1 and m_2 and T_B biases for the remaining seven SMMR channels. In addition, m_1, m_2, and the T_B bias are recomputed for the 18V channel to account for the 18-GHz anomaly. The bias computations are done separately for four time periods and according to descending and ascending orbit segments (i.e., day and night) in order to assess the temporal and day/night stability of the biases. Each time period corresponds to a 24-day portion of the Seasat mission.

We use an iterative procedure in which m_1 and m_2 are first found and then T_B biases are determined. The m_1 and m_2 coefficients are found by inverting (11) such that ΔE is expressed in terms of T_S, W, V, L, and T_{Bi}. A ΔE value is computed for every SMMR cell, giving a total of 116,676 ΔE values for the 3 months. Reynold's climatology is used to specify the sea-surface temperature T_S, and the wind speed W comes from the SASS. The water vapor V and liquid water L are retrieved by the two-channel 21V/37V algorithm, which uses the final values for the T_B bias corrections and coefficients coming from steps 1, 2, and 3. For the first iteration of step 4, the T_B's are not corrected for biases, but in subsequent iterations a bias correction is performed as discussed in the next paragraph. Figures 9 and 10 show ΔE plotted versus the SASS wind speed for the v-pol and h-pol channels, respectively. These figures show the results for the final iteration. The 21-GHz plots, which are not shown, are essentially the same as those for 18 GHz. The ΔE values are put into 1-m/s SASS wind bins, and the dashed curves show the ± 1 standard deviation envelope for the binned ΔE values. The solid curve shows the least squares fit of the ΔE function given by (12) to the ΔE data points. Table 2 gives the m_1 and m_2 coefficients determined from these least squares fits. For the 21V and 37V plots the ΔE data points exactly coincide with the ΔE functions because these channels are used to compute the V and L from which the ΔE data points are then calculated. As a result, the 21V and 37V m's computed in this final step are identical to those coming from step 3 above.

Using the least squares values for m_1 and m_2, the brightness temperature biases ΔT_B are found by computing the average difference between the T_B measurement and the model function.

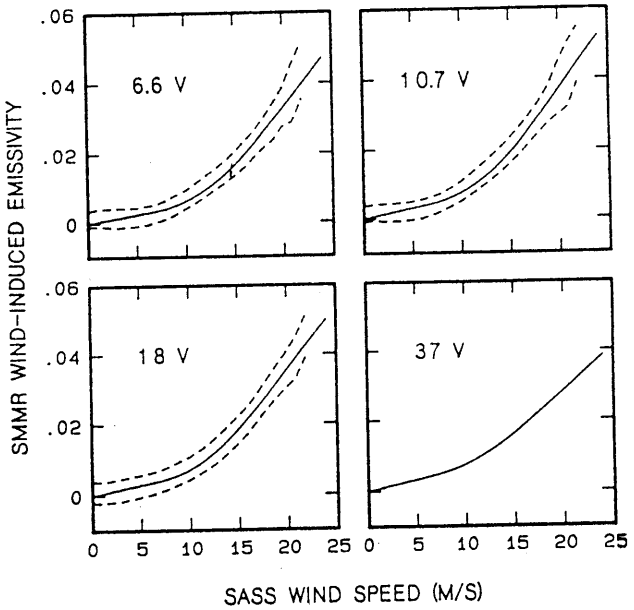

Fig. 9. The wind-induced v-pol sea-surface emissivity derived from collocated SMMR and SASS observations. The solid line represents the mean value, and the dashed curves are the ± 1 standard deviation envelope. Four different SMMR frequencies are shown.

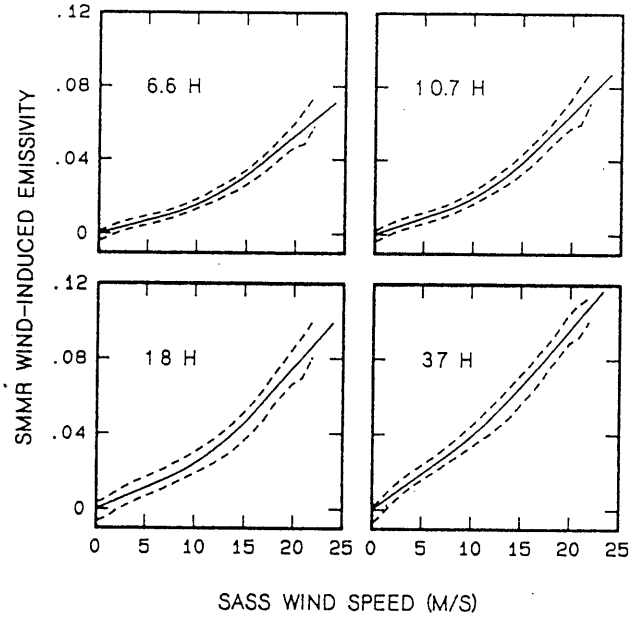

Fig. 10. The wind-induced h-pol sea-surface emissivity derived from collocated SMMR and SASS observations. The solid line represents the mean value, and the dashed curves are the ±1 standard deviation envelope. Four different SMMR frequencies are shown.

$$\Delta T_{Bi} = \langle T'_{Bi} - f_i(T_s, W, V, L) \rangle \qquad (15)$$

where the superscript prime indicates a biased T_B and $\langle \cdots \rangle$ denotes averaging. The averages are stratified according to four 24-day time periods and according to day and night. These biases are subtracted from the T_B measurements, and the m_1 and m_2 coefficients are recomputed. This process is iterated three times to obtain stable values for the m_1 and m_2 coefficients and T_B biases.

Table 3 gives the T_B biases coming from the final iteration. These biases are to be subtracted from the T_B measurements. Except for the 18-GHz channels, the variation in the biases over the four time periods and from day to night is about ±0.5 K. Note that the biases for 21V and 37V are the same as determined from step 1 above, which assumes a constant bias over time and from day to night. This assumption of no temporal drifts for the 21V and 37V channels, which is supported by Figure 8, is necessary because there is no reliable independent information on the temporal variation of water vapor and liquid water. In computing the daytime biases, ocean areas containing sea-surface sun glitter have been excluded. The application of the 18-GHz biases corrects, to a large degree, the anomalous drop in the T_B level, and these channels can now be used to retrieve winds over the entire Seasat 3-month period.

One other aspect of the T_B biases that has not been discussed is the cross-swath biases. The SMMR swath consists of four 150-km-square cells. Stratifying the T_B bias computations according to these four swath positions reveals cell-to-cell relative biases on the order of ±0.5 K. A correction is made for these relative biases.

SMMR Geophysical Retrieval Algorithm

The original SMMR retrieval algorithm [Wentz et al., 1982] used all ten SMMR channels to find T_s, W, V, and L. With ten observations and four unknowns, the inversion problem was overdetermined, and a least squares technique was required to find W, V, L, and T_s. A weight had to be assigned to each channel. This weight represented the inverse of the expected variance between the observation and the model function. To obtain good T_s retrievals, the lower frequency channels needed to be weighted more heavily than the higher frequencies. Although this least squares algorithm performed better than linear regression algorithms [Wentz et al., 1981; Lipes and Born, 1981], it was fairly complex. It was not clear how the 10 channels were affecting the retrieval and what subsets of channels were actually required to accomplish the retrieval. In this sense, the 10-channel algorithm was premature.

A better starting point is to assess the performance of inversion algorithms that use a minimum number of channels. For this investigation, we are primarily interested in wind speed, which can be obtained from just three channels if the sea-surface temperature is specified by climatology. The three channels are required to separate the wind signature from the water vapor and liquid water signatures. Reynolds' [1982] climatology is used to specify T_s. This climatology gives T_s on a 1 month by 1° latitude by 1° longitude grid. The grid values are linearly interpolated in time and space to the center of the SMMR 150-km cell.

A comparison of the winds coming from a three-channel algorithm (6.6H/18V/21V) with those coming from a four-channel algorithm (6.6V/6.6H/18V/21V), which retrieves T_s, shows little difference (0.7-m/s variation) between the two wind estimates. It appears that the climatology T_s is sufficiently accurate to obtain good wind estimates. Note that the rms difference between the climatology T_s and the T_s coming from the four-channel algorithm is only 1.6 C [Wentz, 1983b], which probably explains why the climatology is sufficient. For the SMMR and SASS wind comparisons discussed below, winds are retrieved from eight different combinations of three SMMR channels.

With three observations and three unknowns, the inversion problem is deterministic. If the

TABLE 2. Wind-Induced Emissivity Coefficients

Channel	m_1, s/m	m_2, s/m
6.6V	4.82×10^{-4}	34.07×10^{-4}
6.6H	14.28×10^{-4}	44.85×10^{-4}
10.7V	6.04×10^{-4}	37.32×10^{-4}
10.7H	18.10×10^{-4}	54.76×10^{-4}
18V	6.17×10^{-4}	35.36×10^{-4}
18H	22.06×10^{-4}	60.58×10^{-4}
21V	6.30×10^{-4}	33.72×10^{-4}
21H	24.55×10^{-4}	61.01×10^{-4}
37V	7.00×10^{-4}	25.00×10^{-4}
37H	37.82×10^{-4}	63.27×10^{-4}

TABLE 3. Brightness Temperature Biases in Kelvin for Seasat SMMR

	Night Time Period				Day Time Period			
	1	2	3	4	1	2	3	4
6.6V	-1.5	-0.9	-1.6	-1.7	-1.6	-0.5	-0.2	-.8
6.6H	3.4	3.6	3.2	2.9	3.0	4.2	4.5	3.7
10.7V	-5.8	-6.1	-6.9	-7.0	-6.1	-5.8	-5.8	-6.0
10.7H	-3.9	-4.5	-5.1	-5.2	-4.4	-4.1	-4.0	-4.4
18V	-8.8	-6.7	-11.1	-10.6	-8.7	-8.2	-13.7	-12.6
18H	-1.2	2.2	-3.6	-2.9	-1.5	0.1	-7.2	-6.2
21V	-5.8	-5.8	-5.8	-5.8	-5.8	-5.8	-5.8	-5.8
21H	3.3	2.8	3.2	3.4	2.9	2.2	2.5	2.9
37V	-6.9	-6.9	-6.9	-6.9	-6.9	-6.9	-6.9	-6.9
37H	-1.9	-1.1	-1.1	-0.8	-2.4	-2.3	-2.9	-2.9

T_B function were linear in W, V, and L, the solution could be obtained from a simple 3 by 3 matrix inversion, assuming the matrix is nonsingular. However, because of the nonlinearities, an iterative inversion method must be used. This method is an extension of Newton's method for solving nonlinear equations. In each iteration the following system of three linear equations is inverted:

$$\mathbf{A}\,\mathbf{X} = \mathbf{B} \tag{16}$$

where $\mathbf{A}$ is a 3 by 3 matrix, and $\mathbf{X}$ and $\mathbf{B}$ are three element column vectors. The elements in the unknown vector $\mathbf{X}$ are

$$x_1 = W - W_0 \tag{17a}$$

$$x_2 = V - V_0 \tag{17b}$$

$$x_3 = L - L_0 \tag{17c}$$

where W_0, V_0, and L_0 are first-guess values for the wind speed, water vapor, and liquid water, and W, V, and L are the unknowns to be found. For the first-guess values, we use 7.4 m/s, 2.4 g/cm^2, and 0.01 g/cm^2, respectively. The elements of the $\mathbf{A}$ matrix are derivatives of the SMMR T_B model function $f_i(T_S,W,V,L)$ with respect to W, V, and L.

$$a_{ij} = \partial f_i / \partial x_j \tag{18}$$

These derivatives are computed at the first-guess values. The elements in the vector $\mathbf{B}$ are the differences between the T_B observations and the model function evaluated at the first-guess values.

$$b_i = T_{Bi} - f_i(T_S,W_0,V_0,L_0) \tag{19}$$

Equation (16) is inverted, and values for W, V, and L are obtained. In the second interation, W_0, V_0, and L_0 are set equal to the values coming from the first iteration, and (16) is again inverted. This procedure continues until the W, V, and L values change by less than 0.1% from one iteration to the next. Typically, four or five iterations are required to meet this convergence criteria.

SMMR/SASS Wind Comparisons

The wind speeds coming from the new SASS and SMMR retrieval algorithms are compared on a 150-km cell-by-cell basis over the 3-month Seasat period. For the SMMR wind retrievals, eight different three-channel combinations are considered. Our objective is to determine the optimum channels for a three-channel radiometer system, with an eye toward the new radiometer system SSM/I to be launched in 1986. To obtain the eight different candidate systems, we require that each channel has a high sensitivity to one variable (either W, V, or L) and a relatively low sensitivity to the other two variables. The first channel is the wind speed channel. Since h-pol is much more sensitive to wind speed than v-pol, channel 1 is always h-pol. The second channel is the liquid water channel and must be sensitive to L and insensitive to W. Thus v-pol is always selected for channel 2. Furthermore, since the sensitivity to L increases with frequency, we always choose either 18 and 37 GHz for the liquid water channel. The third channel is the water vapor channel. The obvious selection for this channel is 21V, which is on the water vapor absorption line. This selection procedure yields the following eight three-channel radiometer systems.

1. 6.6H/18V/21V.
2. 6.6H/37V/21V.
3. 10.7H/18V/21V.
4. 10.7H/37V/21V.
5. 18H/18V/21V.
6. 18H/37V/21V.
7. 37H/18V/21V.
8. 37H/37V/21V.

The SSM/I will not have the two lower frequency channels, 6.6H and 10.7H, but will have channels closely corresponding to the three higher frequencies. Furthermore, the SSM/I incidence angle of 53° is close to SMMR's 49° incidence angle. Thus the wind retrievals coming from combinations 5 through 8 will be indicative of the SSM/I wind-sensing capability.

On Seasat, the swaths for the SASS and SMMR overlap on the starboard side of the satellite subtrack. As shown in Figure 11, the overlap area extends 600 km out from the subtrack and is divided into four 150-km-square resolution cells, which correspond to the resolution of the SMMR's

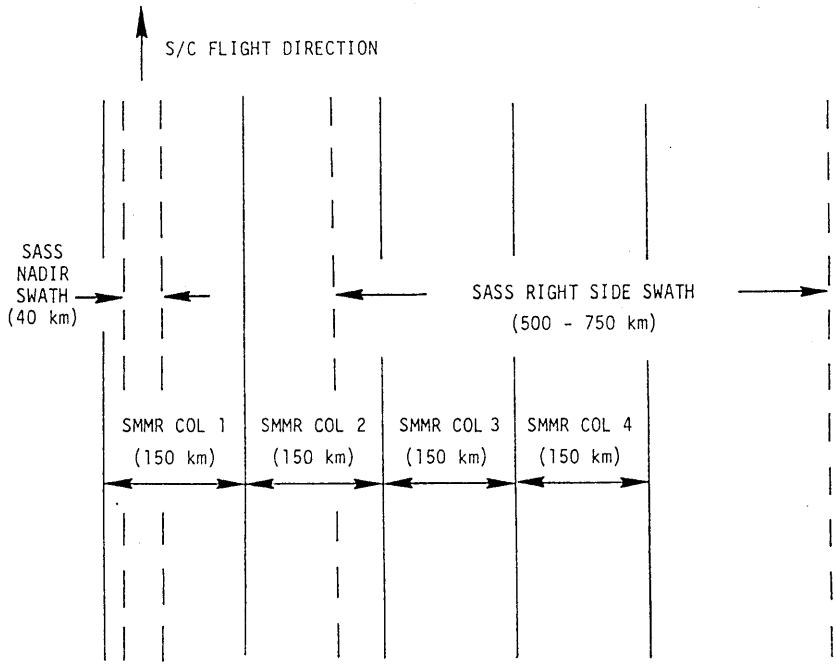

Fig. 11. The geometry of the SMMR and SASS overlapping swaths.

lowest frequency channels at 6.6 GHz. Beginning with the subtrack cell, these cells are numbered 1 through 4. The T_B measurements uniformly cover each cell, but the SASS σ^0 measurements do not. For cell 1, we use only the nadir SASS measurements that are restricted to a 40-km-wide strip along the subtrack. The near-nadir SASS measurements at incidence angles of 4° and 8° are not used because they are relatively insensitive to wind speed. Cell 2 is also only partially filled with SASS observations. There is a gap in the SASS swath for incidence angles between 10° and 20°, and as a result the left half of cell 2 does not contain any SASS observations. The outer cells 3 and 4 are completely within the SASS primary swath and are uniformly filled with SASS measurements. The SASS winds are computed on a 100-km grid system aligned to the satellite subtrack. In order to associate a SASS wind with each SMMR 150-km cell, we average together winds from all SASS cells having a center point within a 200-km radius of the SMMR cell center. When averaging SASS winds, a $1/R^2$ weighting is used, where R is the distance between the SASS and the SMMR cell.

The SMMR antenna does a conical scan such that the incidence angle is a constant 49°. Thus the same physics and model function applies to cells 1 through 4. The only difference is that significant polarization coupling occurs for the edge cells 1 and 4. This polarization coupling makes the decoupled T_B values noisier for the edge cells. In contrast, the SASS antennas are fixed sticks, and each cell corresponds to a different range of incidence angles. The SASS measurements in cell 1 are nadir observations for which σ^0 decreases with wind speed W approximately as $(1/W)^{\frac{1}{2}}$. For cell 2 the average incidence angle is about 24°, and σ^0 increases linearly with wind speed. For the two outer cells, the average incidence angles are 34° and 45°, and σ^0 increases as the square of wind speed. Thus the SASS model function is quite different for the four cells. In view of this, the SMMR/SASS wind comparisons are stratified according to cell number. We expect that the best comparisons will occur for cell 3. For this cell, there is uniform coverage of both T_B and σ^0 observations, the signal-to-noise ratio for SASS is the best, σ^0 is most sensitive to wind speed, and the polarization coupling in the T_B's is a minimum.

The following objective criteria are used to quality filter the T_B's used in the SMMR/SASS wind comparisons. Only nighttime observations are used because sea-surface sun glitter and Faraday rotation degrade the daytime T_B data at 6.6 and 10.7 GHz. Furthermore, we require that the T_B observations be at least 800 km from land in order to avoid antenna sidelobe contamination at 6.6 and 10.7 GHz. As a final filtering criteria, SMMR cells containing rain are excluded. Rain is indicated when the liquid water content L exceeds 34 mg/cm². This rain filter excludes about 2% of the cells. The exclusion of daytime data is probably not necessary for the radiometer systems 5 through 8, which do not use the 6.6 of 10.7-GHz channels. Likewise, the restriction of being 800 km away from land could be substantially relaxed for the higher frequency systems. However, to maintain the same data base when comparing the eight different systems, we use the same filtering criteria for all systems.

Table 4 gives the standard deviation of the SMMR minus SASS wind difference for the various candidate systems and for cells 1 through 4. The mean SMMR minus SASS wind difference is within ±0.1 m/s for all cases, except for the two poorly performing systems mentioned below. For each of the four cells, the number of SMMR/SASS wind pairs that went into the statistics is about 30,000. Six radiometer systems provide winds that are in good agreement with the SASS winds, while two systems, 18H/18V/21V and 37H/18V/21V, show little and no skill, respectively, in re-

TABLE 4. Standard Deviation of SMMR-SASS Wind Comparisons in Meters per Second

System	Cell 1	Cell 2	Cell 3	Cell 4
6.6H/18V/21V	1.6	1.4	1.4	1.5
6.6H/37V/21V	1.5	1.3	1.3	1.4
10.7H/18V/21V	1.9	1.8	1.8	2.0
10.7H/37V/21V	1.5	1.4	1.4	1.5
18H/18V/21V	4.1	3.0	3.0	3.4
18H/37V/21V	2.5	2.2	2.2	2.3
37H/18V/21V	5.5	5.6	5.6	5.7
37H/37V/21V	2.0	1.7	1.7	1.8

trieving wind. As will be shown, the poor results for these two systems are due to a near singularity in A-matrix in (16) of the inversion algorithm. The best three systems are 6.6H/18V/21V, 6.6H/37V/21V, and 10.7H/37V/21V, for which the SMMR/SASS agreement is about 1.4 m/s for cells 2 through 4, which cover the SASS primary off-nadir swath. The SMMR/SASS agreement is slightly degraded for the SASS nadir cell 1. The performance of the other three systems, 10.7H/18V/21V, 18H/37V/21V, and 37H/37V/21V is somewhat poorer, with the rms variation being about 2 m/s. Note that the performance statistics obtained for the 18H/37V/21V system may be an underestimation of its actual capabilities because of the problems experienced by SMMR's 18-GHz channels.

Figure 12 shows the SMMR minus SASS wind speed difference plotted versus the SMMR and SASS wind speed average. Twenty-four separate plots are shown corresponding to the six radiometer systems and the four cells across the swath. The solid curve is the mean of the SMMR minus SASS difference, and the dashed lines are the ± 1 standard deviation envelope for the wind differences. From 3 to 17 m/s the curves are quite flat, and very good agreement is obtained. For winds below 3 m/s, the SMMR winds are consistently less than the SASS winds. The SMMR winds appear to be more noisy than the SASS winds at these low wind speeds. They have negative values (-1 to -3 m/s) more often than the SASS winds, and these negative winds bias the SMMR winds low compared with the SASS winds. For winds above 17 m/s, the SMMR winds are systematically higher than SASS. It is unclear which sensor is more correct at these high winds.

The performance of the eight radiometer systems is explained by an error analysis of the retrieval algorithm given by (16) through (19). These equations are used to map the errors in the T_B measurements into a wind speed error. Table 5 gives the predicted wind speed error assuming a 0.5 K zero-mean Gaussian error in the brightness temperatures. The errors for each channel are assumed uncorrelated. Considering the antenna temperature resolution for SMMR [Njoku et al., 1980b], the 0.5 K error is a reasonable assumption for the 150-km cells. To compute these errors, nominal values for T_S, W, V, and L must be assigned. The values for T_S, V, and L are 290 K, 2.4 g/cm^2, and 10 mg/cm^2, respectively. Because of the nonlinearity in the T_B versus wind speed dependence, two values for wind speed are considered: 7 and 15 m/s. These predicted errors show the same trends that are observed in the SMMR/SASS wind comparisons. All systems have wind speed errors less than 2 m/s, except 18H/18V/21V and 37H/18V/21V, for which the A-matrix in (16) is nearly singular. The response of the h-pol T_B to wind speed is greater at 15 m/s than at 7 m/s, and hence the predicted wind speed error is smaller for the higher wind speed case, except for the two poorly performing systems and the 37H/37V/21V system. For these three systems the determinant of the A-matrix decreases in spite of the increase in the h-pol T_B response. Figure 12 also shows this tendency of the 37H/37V/21V system to give more noisy retrievals at the higher winds.

With respect to the possible SSM/I channel combinations, Table 5 indicates that 18H/37V/21V is preferable to 37H/37V/21V, whereas the SMMR/SASS wind comparisons indicate 37H/37V/21V is the better choice for wind speeds below 10 m/s. The 37H/37V/21V system performs better with real data probably because it relies on a single frequency to separate wind from liquid water, whereas the 18H/37V/21V utilizes two frequencies. The 37H and 37V channels have the same atmospheric absorption coefficients. In contrast, there is not a fixed relationship between the 18- and 37-GHz absorption coefficients for liquid water. The cloud and raindrop size distribution, the temperature of the water droplets, and the horizontal distribution of the liquid water over the SMMR cell all affect the frequency dependence of the averaged atmospheric absorption for a SMMR cell. The T_B model does not account for these effects.

At the higher wind speeds, Figure 12 shows that the 18H/37V/21V performs slightly better. Also, the 18-GHz channels on SMMR experienced calibration problems, and the true capability of the 18H/37V/21V system may be better than is indicated here. Possibly a combination of 18H, 37H, 37V, and 21V may prove best for retrieving winds from SSM/I. In any event, the results do indicate that the SSM/I will have the capability to measure the near-surface wind speed to an accuracy of about 2 m/s, or possibly better. However, we point out that the analysis herein is all done at a 150-km resolution. The impact of resolution on wind accuracy is an important question that needs further study.

Comparison of SMMR and SSM/I Instrumentation

In 1986, the first in a new generation of satellite microwave radiometers will be launched aboard the Defense Meteorological Satellite Program (DMSP) Block 5D-2 spacecraft. The SSM/I is a four-frequency, conical scanning radiometer that will measure the brightness temperature of the earth's surface and the intervening atmosphere. Its four frequencies are 19.3, 22.2, 37.0, and 85.5 GHz. Each frequency has a horizontal and vertical polarization channel except 22.2 GHz, which has only a v-pol channel. The instrument will be in a sun-synchronous orbit at an altitude of 833 km with a 98.7° inclination. The earth incidence angle will be 53.1°, and the swath width will be 1390 km. The parabolic reflector has a 0.6-m diameter, which will result

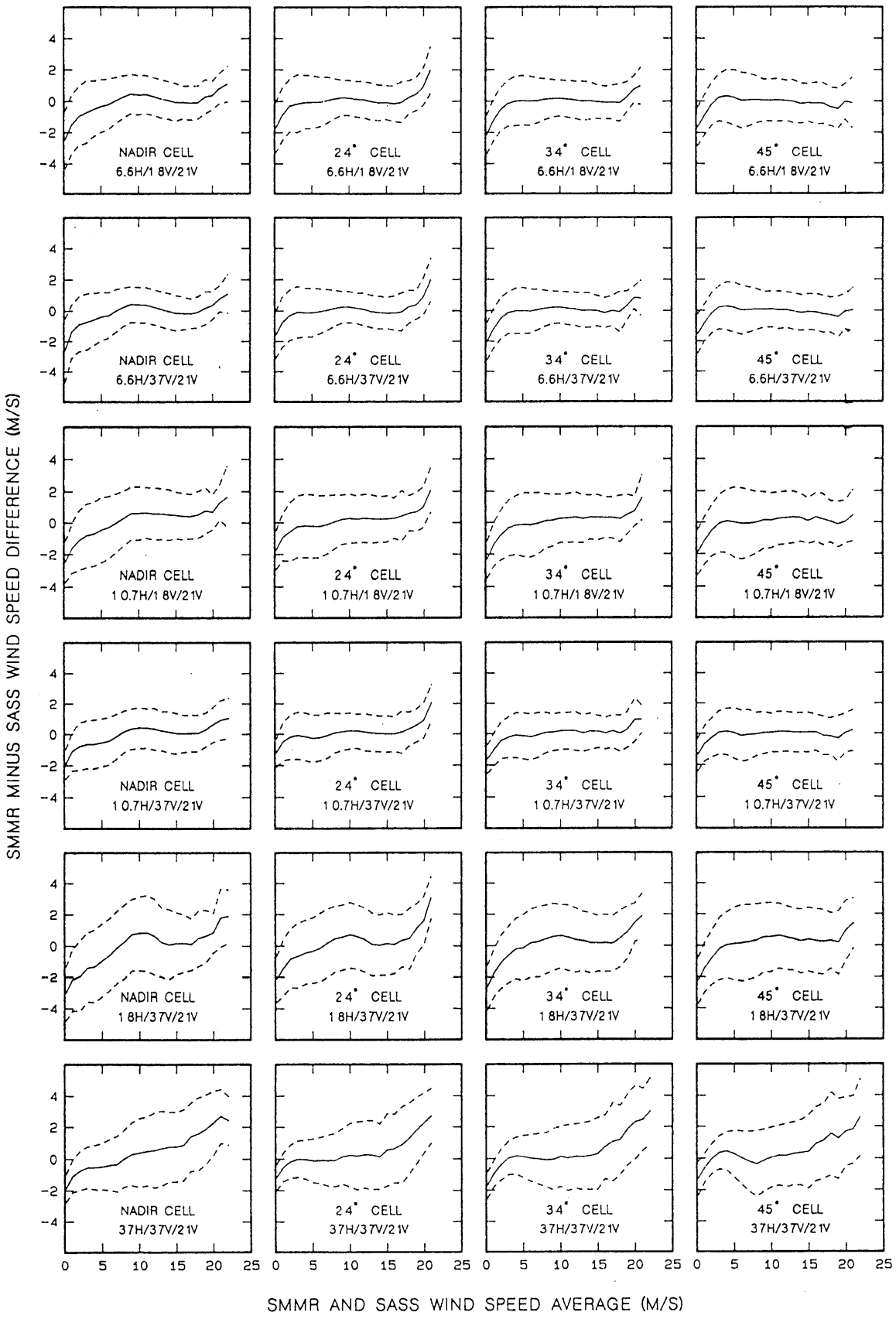

Fig. 12. A comparison of SASS winds with winds coming from six different combinations of three SMMR channels. Each row of plots corresponds to a different three-channel system. The four plots in a row correspond to the four cells across the SMMR swath. The average SASS incidence angle for each cell is shown.

TABLE 5. Predicted Wind Retrieval Errors in Meters per Second Assuming a 0.5 K Error in Brightness Temperature

	Wind Speed	
	7 m/s	15 m/s
6.6H/18V/21V	1.4	0.6
6.6H/37V/21V	1.3	0.5
10.7H/18V/21V	1.5	0.8
10.7H/37V/21V	1.0	0.4
18H/18V/21V	2.5	4.8
18H/37V/21V	1.2	0.7
37H/18V/21V	9.8	9.8
37H/37V/21V	1.5	1.8

in a cell resolution between 15 and 50 km, depending on frequency. A more complete description of the SSM/I hardware is given by Hollinger and Lo [1983].

SSM/I is an improvement over its predecessors, the Seasat and NIMBUS 7 SMMR's. The improved hardware design should greatly mitigate the bias problem that occurred for the SMMR's. SSM/I is a total power radiometer having a single feed-horn. The entire sensor (i.e., radiometer and parabolic reflector) spins at a rate of one revolution every 1.9 s. An external cold-space reflector and warm reference load, which are mounted on the spin axis and do not rotate, occult the spinning feed-horn once each revolution. In this way, a cold and warm reference voltage is obtained every 1.9 s through a single feed-horn. In contrast, the SMMR had a separate feed-horn to view cold space and utilized an internal termination load to obtain a warm reference voltage. Ferrite switches were used to connect the Dicke switch to the earth-viewing feed-horn, the cold-space feed-horn, and the internal warm reference load. Thus radiation coming from these three sources traveled along separate waveguide paths and through various ferrite switches. Due to this arrangement, the volt-to-T_A transfer function was quite sensitive to temperature differences along the various transmission paths. Furthermore, this calibration scheme required a high degree of reliability for the ferrite switches; i.e., their transmission properties needed to stay constant over the life of the sensor. The SMMR calibration design was further complicated by the fact that different cold-space horns and ferrite switches were used for different channels. The end result appears to have been poorly calibrated T_A's due to the thermal gradients within the radiometer and degrading ferrite switches. The T_B biases shown in Table 3 attest to these calibration problems.

In addition to the improved volt-to-T_A calibration, the SSM/I antenna scanning mechanism maintains a constant alignment between the antenna polarization vectors and the earth's h-pol and v-pol vectors. This is a direct consequence of the feed-horn and parabolic reflector spinning as a unit. In comparison, the SMMR's parabolic reflector was mechanically scanned while the feed-horn remained fixed. This resulted in the h-pol and v-pol earth polarization vectors rotating relative to the fixed polarization vectors of the feed-horn. This rotation of polarization vectors greatly complicated the data processing and was probably the cause for the cross-swath biases.

The simple design of SSM/I will be a welcome improvement. The cross-swath, temporal, and day/night biases that SMMR experienced should be greatly reduced, leaving only an absolute bias to deal with. The one major drawback to SSM/I is that it is missing the SMMR's two lower frequencies of 6.6 and 10.7 GHz. This will make viewing the earth's surface more difficult when heavy clouds and rain are present. Also, the absence of the lower frequencies will prohibit the SSM/I from measuring the sea-surface temperature.

Summary and Conclusions

A new NRCS model and wind retrieval algorithm are derived for the Seasat SASS. The derivation of the NRCS model is based on the assumption of a Rayleigh distribution of wind speeds, and no in situ anemometer measurements are used. Furthermore, the derivation is designed to preclude, as much as possible, systematic polarization and incidence angle errors in the retrieved wind speeds. We verify the derivation by comparing wind speeds computed from different σ^0 polarizations and incidence angles. These comparisons show a very close agreement, although small residual systematic errors are still apparent. The h-pol versus v-pol wind comparisons show a systematic error having an amplitude of about ± 0.5 m/s over the 0- to 20-m/s range. The amplitude of this systematic error grows with incidence angle. The adjacent cell comparisons (i.e., different incidence angles) show a small ± 0.2 m/s systematic error. These systematic errors in winds from the port side of the satellite subtrack are nearly identical to those shown by the starboard winds. The cause of these errors is not known. For most applications they will be of little consequence.

The nadir NRCS for winds above 15 m/s appears to fall off faster with increasing wind speed than is predicted by a constant power law relationship. To account for this, a finely incremented table for relating the nadir NRCS to wind speed is computed.

The distribution of SASS winds for the 3-month Seasat period is similar to a Rayleigh probability density function. Thus the initial assumption of a Rayleigh distribution of wind speeds is self-consistent. The rms discrepancy between 1623 SASS and buoy wind speeds is 1.6 m/s, with a -0.1-m/s bias. This good agreement supports the statistical assumptions in the derivation and our assertion that accurate models and algorithms can be developed without using in situ observations.

The derivation of the new SMMR T_B model and geophysical retrieval algorithm involves determining the biases in the T_B observations, the wind-induced emissivity coefficients, and the 37-GHz atmospheric absorption coefficients. Except for the 18-GHz channels, the magnitude of T_B biases ranges from 1 to 7 K, depending on the channel. The biases for the daytime portion of an orbit are slightly different (0.5 to 1 K) from those for the nighttime orbit segment. In addi-

tion, there is about a ±0.5 K variation in the biases when they are stratified according to four 24-day time periods. Small cross-swath biases on the order of ±0.5 K also occur. The biases for 18-GHz channels are larger. A sudden 5 K drop in the mean level of the 18-GHz v-pol and h-pol channels occurred at the end of August 1978.

The wind-induced emissivity coefficients in the SMMR T_B model are derived from collocated SASS wind speeds. The slope of the wind-induced emissivity versus wind speed increases with wind speed, indicating a nonlinear relationship. At 37 GHz, the theoretical absorption coefficients for water vapor and liquid water are reduced by a factor of 0.88 and 0.73, respectively, in order to obtain consistency between the liquid water contents inferred from the 18V and 21V channels and those inferred from the 37V and 21V channels. It is not clear why the theoretical coefficients gave inconsistent liquid waters. Some possible explanations are rain cells that are small compared with the resolution cell size, Mie scattering, or an incorrect specification of the temperature profile for the liquid water.

The winds coming from the microwave radiometer SMMR and the microwave scatterometer SASS are compared and found to be highly correlated. Three of the SMMR channel combinations considered (6.6H/18V/21V, 6.6H/37V/21V, 10.7H/37V/21V) produce winds that show a 1.4-m/s agreement with the off-nadir SASS winds. For the nadir SASS winds, the agreement slightly degrades to 1.6 m/s. A second set of channel combinations (10.7H/18V/21V, 18H/37V/21V, 37H/37V/21V) performs nearly as well, showing about a 2-m/s SMMR/SASS discrepancy. The final two SMMR channel combinations that are considered (18H/18V/21V, 37H/18V/21V) demonstrate little, if any, skill in retrieving wind speed.

The SMMR winds appear to be more noisy than the SASS winds for winds below 3 m/s. For winds above 15 m/s, the SMMR winds are systematically higher than the SASS winds by about 1 to 2 m/s. The good agreement that is obtained for winds from 3 to 7 m/s indicates that the SMMR brightness temperatures are sensitive to wind speed via wave tilting when there is little or no whitecapping.

The results for the 18H/37V/21V and 37H/37V/21V SMMR versus SASS comparisons indicate that upcoming satellite microwave radiometer SSM/I, to be launched in 1986, will have the capability to measure the near-surface wind speed with about a 2-m/s accuracy.

There are a number of questions that still need to be addressed concerning the capabilities of SMMR, SASS, SSM/I, and the microwave sensors to be flown on the Navy's Remote Ocean Sensing System (N-ROSS). The investigation reported herein only considers SASS winds at a 100-km resolution and SMMR winds, water vapors, and liquid water contents at a 150-km resolution. Many applications such as storm research require a finer resolution such as 25 or 50 km. The microwave signature of rain bands, which are typically 5 to 10 km in size, will be more dominant at the finer resolutions and will interfere with the wind retrievals. Furthermore, the scatterometer and radiometer noise will be greater because the temporal and spatial time averages will be smaller. To address these resolution questions, we plan to retrieve wind speeds, water vapors, and liquid water contents from the 50-km resolution SMMR T_B's and SASS σ^o's.

One very important problem that is not addressed in this investigation is the retrieval of wind direction from scatterometer measurements. We consider the wind direction retrieval problem an open issue that needs considerably more investigation.

In conclusion, we encourage other investigators to use the new second-generation SMMR and SASS geophysical data products, which are a substantial improvement over the first-generation products released in 1981. These data are available in a convenient, compact format.

Acknowledgments. The reprocessing of the Seasat data and subsequent analysis were funded by NASA's Oceanic Processes Program under contract NASW-3606. We are very grateful for NASA's interest and continuing support of this research. Additional support was provided by the Canadian Atmospheric Environment Service and by NORDA's Remote Sensing Branch under contract N00014-83-C-0520. We thank L. McGoldrick and W. Patzert of NASA Headquarters and J. Hawkins of NORDA for sponsoring this study. We also thank D. Chelton for providing the NDBO buoy observations.

References

Alishouse, J. C., Total precipitable water and rainfall determinations from the Seasat scanning multichannel microwave radiometer, J. Geophys. Res., 88(C3), 1929-1935, 1983.

Barrett, A. H., and V. K. Chung, A method for the determination of high-altitude water vapor abundance from ground-based microwave observations, J. Geophys. Res., 67, 4259-4266, 1962.

Bernstein, R. L. (Ed.), Seasat Special Issue 1, J. Geophys. Res., 87(C5), 3173-3438, 1982.

Bernstein, R. L., and J. H. Morris, Tropical and mid-latitude North Pacific sea surface temperature variability from the Seasat SMMR, J. Geophys. Res., 88(C3), 1877-1891, 1983.

Brown, R. A., V. J. Cardone, T. Guymer, J. Hawkins, J. E. Overland, W. J. Pierson, S. Peteherych, J. C. Wilkerson, P. M. Woiceshyn, and M. Wurtele, Surface wind analyses for SEASAT, J. Geophys. Res., 87(C5), 3355-3364, 1982.

Cardone, V., T. Chester, and R. Lipes, Evaluation of Seasat SMMR wind speed measurements, J. Geophys. Res., 88(C3), 1709-1726, 1983.

Chelton, D. B., and P. J. McCabe, A review of satellite altimeter measurements of sea surface wind speed: With a proposed new algorithm, J. Geophys. Res., 90(C3), 4707-4720, 1985.

Hollinger, J. P., and R. C. Lo, SSM/I project summary report, NRL Memo. Rep. 5055, 106 pp., Nav. Res. Lab., Washington, D. C., April 1983.

Jones, W. L., and L. C. Schroeder, Radar backscatter from the ocean: Dependence on surface friction velocity, Boundary Layer Meteorol., 13, 133-149, 1978.

Jones, W. L., L. C. Schroeder, D. H. Boggs, E. M. Bracalente, R. A. Brown, G. J. Dome, W. J. Pierson, and F. J. Wentz, The Seasat-A satellite scatterometer: The geophysical evaluation of remotely sensed wind vectors over the

ocean, J. Geophys. Res., 87(C5), 3297-3317, 1982.

Kinsman, B., Wind Waves, Their Generation and Propagation on the Ocean Surface, Prentice-Hall, Englewood Cliffs, N. J., 1965.

Lipes, R. G., and G. H. Born (Eds.), SMMR mini-workshop IV, JPL Tech. Rep. 622-234, Jet Propul. Lab., Pasadena, Calif., 1981.

Munn, R. E. (Ed.), Special Issue: IUCRM Colloquium on 'Radio Oceanography', Boundary Layer Meteorol., 13, 1-429, 1978.

Njoku, E. G., E. J. Christensen, and R. E. Cofield, The Seasat scanning multichannel microwave radiometer (SMMR): Antenna pattern corrections-development and implementation, IEEE J. Oceanic Eng., OE-5(2), 125-137, 1980a.

Njoku, E. G., J. M. Stacy, and F. T. Barath, The Seasat scanning multichannel microwave radiometer (SMMR): Instrument description and performance, IEEE J. Oceanic Eng., OE-5, 100-115, 1980b.

Nordberg, W., J. Conaway, D. B. Ross, and T. Wilheit, Measurements of microwave emission from a foam-covered wind driven sea, J. Atmos. Sci., 38, 429-435, 1971.

Reynolds, R. W., A monthly averaged climatology of sea surface temperature, NOAA Tech. Rep. NWS 31, Nat. Weather Serv., Silver Spring, Md., 1982.

Schroeder, L. C., D. H. Boggs, G. Dome, I. M. Halberstam, W. L. Jones, W. J. Pierson, and F. J. Wentz, The relationship between wind vector and normalized radar cross section used to derive Seasat-A satellite scatterometer winds, J. Geophys. Res., 87(C5), 3318-3336, 1982.

Swift, C. T. (Ed.), Special Joint Issue on Radio Oceanography, IEEE J. Oceanic Eng., OE2, 1-159, 1977.

Weissman, D. E. (Ed.), Special Issue on the Seasat-1 Sensors, IEEE J. Oceanic Eng., OE5, 71-182, 1980.

Weller, R. A., R. E. Payne, W. G. Large, and W. Zenk, Wind measurements from an array of oceanographic moorings and from F/S Meteor during JASIN 1978, J. Geophys. Res., 88, 9689-9705, 1983.

Wentz, F. J., A model function for ocean microwave brightness temperatures, J. Geophys. Res., 88(C3), 1892-1908, 1983a.

Wentz, F. J., Comparison of sea surface temperature retrievals using 6.6 and 10.7 GHz, RSS Tech. Rep. SSD 10020, 28 pp., Remote Sensing Syst., Sausalito, Calif., Sept. 1983b.

Wentz, F. J., E. J. Christensen, and K. A. Richardson, Comparison of Seasat SMMR geophysical algorithms, RSS Tech. Rep. 954958, 18 pp., Remote Sensing Sys., Sausalito, Calif., June 1981.

Wentz, F. J., V. J. Cardone, and L. S. Fedor, Intercomparison of wind speeds inferred by the SASS, altimeter, and SMMR, J. Geophys. Res., 87(C5), 3378-3384, 1982.

Wentz, F. J., S. Peteherych, and L. A. Thomas, A model function for ocean radar cross sections at 14.6 GHz, J. Geophys. Res., 89(C3), 3689-3704, 1984.

Wilheit, T. T., and A. T. C. Chang, An algorithm for retrieval of ocean surface and atmospheric parameters from the observations of the scanning multichannel microwave radiometer, Radio Sci., 15, 525-544, 1980.

Woiceshyn, P. M., M. G. Wurtele, D. H. Boggs, L. F. McGoldrick, and S. Peteherych, The necessity for a new parameterization of an empirical model for wind/ocean scatterometry, J. Geophys. Res., this issue.

L. A. Mattox and F. J. Wentz, Remote Sensing Systems, 475 Gate Five Road, Suite 211, Sausalito, CA 94965.

S. Peteherych, Atmospheric Environment Service, 4905 Dufferin Street, Downsview, Ontario, Canada M3H5T4.

(Received November 20, 1984;
accepted January 23, 1985.)